ELSEVIER

Contents lists available at ScienceDirect

Materials Science & Engineering A

journal homepage: www.elsevier.com/locate/msea





Creep property and microstructural evolution of laser powder bed fused binary Al–10Ce alloy

Jillian Stinehart^a, Luis Fernando Ladinos Pizano^b, Wei Xiong^b, Le Zhou^{a,*}

- ^a Department of Mechanical Engineering, Marquette University, Milwaukee, WI, 53233, USA
- ^b Department of Mechanical Engineering and Materials Science, University of Pittsburgh, Pittsburgh, PA, 15261, USA

ARTICLE INFO

Keywords:
Laser powder bed fusion (LPBF)
Aluminum-cerium (Al–Ce)
Creep
Microstructure

ABSTRACT

Aluminum–Cerium (Al–Ce) based alloys have shown promise as cost-efficient high temperature creep-resistant aluminum alloy. These alloys are also highly printable with laser powder bed fusion (LPBF) additive manufacturing. This study investigates the creep property of a near eutectic binary Al–10Ce (wt. %) alloy manufactured by LPBF and its microstructural evolution during creep. The as-built alloy exhibited columnar grain structure with a weak cube texture and its microstructure consisted of fine eutectic Al + Al₁₁Ce₃. Compressive creep tests with incremental stresses were performed perpendicular to the build direction at temperatures ranging from 275 to 400 °C. The stress exponent was approximately 1 in the low stress regime and 5–7 in the high stress regime, corresponding to diffusion and dislocation creep, respectively. The average activation energy was approximately 229 kJ/mol·K in the temperature between 275 and 375 °C. After creep deformation, the melt pool boundary faded and the eutectic Al₁₁Ce₃ intermetallics slightly coarsened. The grain structure remained relatively stable and the grain boundary became more pronounced. By comparing the minimum creep strain rate to other alloys, it was found that LPBF Al–10Ce is more creep resistant than similar cast binary Al–Ce counterpart, some ternary Al–Ce alloys and LPBF AlSi10Mg alloy. This benchmark results on the creep property of LPBF binary eutectic Al–Ce alloy provide insights to future development of creep-resistant Al–Ce alloys.

1. Introduction

Currently, few commercial aluminum alloys (AAs) are available for high-temperature applications. While cast aluminum-silicon (Al–Si) based alloys and wrought 6xxx or 7xxx alloys exhibit high strength at room temperature due to precipitation hardening, their strength degrades rapidly with increasing temperature and over time because of microstructural and precipitate coarsening. To retain the high temperature strength, scandium (Sc) and zirconium (Zr) among others have been used as alloying elements [1]. These elements can form L1₂ Al₃X type of trialuminide, which exhibit slow coarsening kinetics and provide precipitation strengthening at high temperature [2]. Aluminum-iron based alloys with large volume fraction of fine precipitates manufactured through powder metallurgy thermomechanical processing have also been developed for high temperature applications [3].

Recently, aluminum-cerium (Al–Ce) based near-eutectic alloys have been gained more attention due to their outstanding microstructural stability and capability to retain strength after high temperature exposure [4–6]. Earlier development of Al–Ce alloys started with

melt-spinning technique to fabricate alloy ribbons [7] while recent studies focused on alloy development for cast alloys with improved mechanical property [8]. Several rationales and advantages to justify the use of Ce in Al include but not limited to: (1) Ce has limited solubility and slow diffusivity in Al matrix, which contributes to the thermal stability; (2) Similar to Si, Ce improves the castability of Al alloys; (3) Ce reduces the intergranular corrosion of Al alloys; (4) The price of Ce is much lower than many other rare earth elements (e.g., Sc) for high temperature Al alloys; (5) Ce is the most abundant rare earth elements on the earth crust but is often discarded as byproduct waste [9]. Utilization of Ce in Al therefore will not only improve the high temperature properties, but also have economic and environmental benefits. On the other hand, Ce alone has limited effect in improving the strength of the Al alloys owing to its limited solubility. Therefore, alloy development is still needed to further strengthen the Al-Ce alloy. Several research studies have been devoted to developing ternary or higher order Al-Ce based alloys and show promise. Alloys including Al-Ce-Mg [4,10], Al-Ce-Ni [11], Al-Ce-Cu [12], Al-Ce-Mg-Si [13], have been investigated. Notably, Mg has been the most common alloying elements added to

E-mail address: le.zhou@marquette.edu (L. Zhou).

 $^{^{\}ast}$ Corresponding author.

Al–Ce alloys. It contributes to strength through solid solution strengthening and is the most effective strengthening alloying elements on weight basis [10].

Metal additive manufacturing (AM) research is growing tremendously recently, and there is a desire for printable materials that are lightweight and can be used in high temperature environments. Many commercial AAs face issues such as solidification cracking after AM, especially when processed by laser powder bed fusion (LPBF). To resolve the solidification cracking and improve the printability of AAs, two alloy design strategies have been proposed: refining the solidification grains by alloying with grain refining elements (e.g., Sc or Zr) [14-16] or designing compositions with eutectic solidification to reduce the solidification range and cracking tendency [17]. Inherently, Al-Ce alloys exhibit a eutectic reaction at near 10 wt% of Ce, at which the solidification cracking tendency based on Kou's theory is expected to be low [18]. Several recent studies have further shown that binary and ternary Al-Ce based alloys can be manufactured by LPBF without the issue of solidification cracking [19-22]. Moreover, the refined eutectic microstructure improves the strength of the Al-Ce alloys compared to their cast counterparts.

Creep is an important property to consider for materials used at high temperatures. Recent studies have shown that Al–Ce based alloys exhibit outstanding creep resistance at high temperatures. Liu et al. showed that the creep property of cast Al-12.5Ce is better than that of Al-Sc-Zr-based alloys and comparable to Al–Ni-based alloys [23]. The capability of Al₁₁Ce₃ intermetallic to transfer load and obstruct dislocation climb contributes to the alloy's creep resistance. Ng et al. reported the creep resistance of cast ternary Al–Ce–Mg alloy, which is inferior to the binary Al–Ce alloy [24]. The creep property of Al–Ce alloys manufactured by LPBF has also been studied recently, all of which exhibit superior creep resistance compared to the cast counterparts [25,26]. It is noted that the alloys in these studies focused on ternary or higher-order Al–Ce alloys. As also pointed out by Rakhmonov et al. [25], there is still a need to better understand the creep behavior of the baseline LPBF binary Al–Ce alloy.

The primary objective of this study is to investigate the creep property and microstructural evolution of an LPBF binary Al–10Ce alloy. This study will report a benchmark result for the binary Al–Ce alloy manufactured by LPBF, which will provide insights to its fundamental creep deformation and implications on future alloy design based on Al–Ce alloys.

2. Experimental procedures

2.1. Materials

Samples with Al-10Ce (wt. %) compositions were manufactured from gas-atomized powders using a SLM125HL (SLM Solutions, Germany) LPBF system equipped with a single (400 W) IPG fiber laser with a laser beam focus diameter of approximately 70 μm. Two rectangular bars with a dimension of 10 mm \times 10 mm \times 80 mm were manufactured horizontally with respect to the build plate, i.e., the XY plane as shown in Fig. 1(a). The processing parameters used include a laser power of 350 W, a scan speed of 1400 mm/s, a hatch spacing of 0.13 mm and a layer thickness of 0.03 mm. The density of the LPBF sample was approximately 99.8% at these parameters [27]. Details of the processing can be found in Ref. [27]. The actual composition of the samples is measured by energy dispersive spectroscopy (EDS) and determined to be Al-10.56 wt %Ce by averaging over ten different areas on the cross-sections. The rectangular bars were machined into several cylindrical specimens with a diameter of 8 mm and a height of 16 mm for subsequent compressive creep tests. The top and bottom surfaces of the cylinders were ground using a SiC sandpaper (1200 grit) to ensure that the two surfaces were planar and parallel.

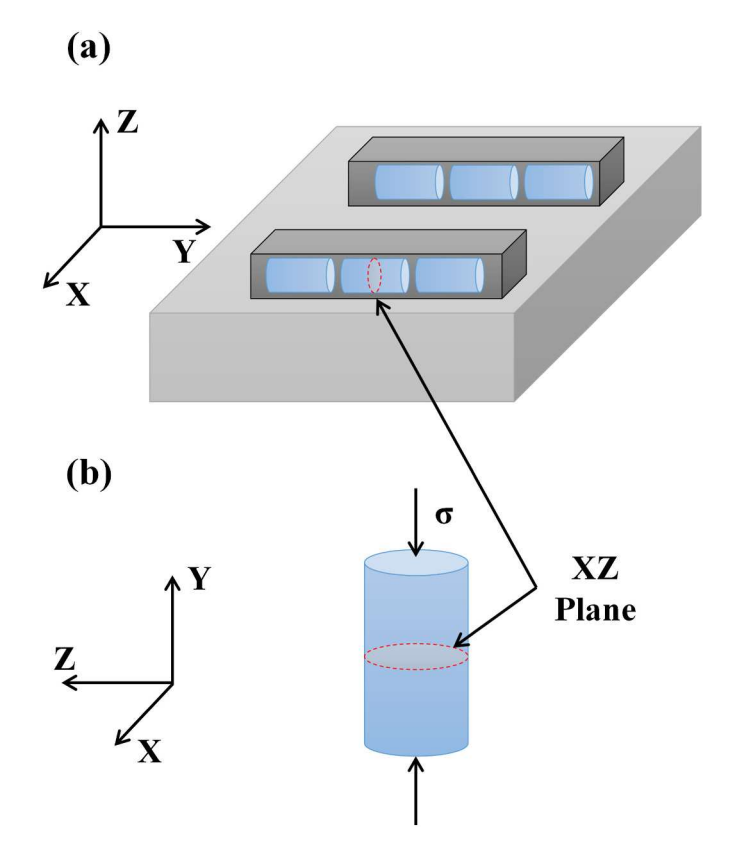


Fig. 1. Schematic illustration of (a) the build direction of the Al–10Ce bars and (b) the creep loading direction with respect to the build direction.

2.2. Compressive creep test

A dead-weight lever arm creep test system (Applied Test Systems, USA) was used for all creep tests. A 3-zone furnace equipped with K-type thermocouples was used to control the test temperature. Power was run from a 208V outlet and connected to three temperature controllers. Each temperature controller supplied power to one zone of the furnace, and the temperature was controlled within $\pm 2\,^\circ\text{C}$ of the setpoint temperature in accordance with ASTM E139-11. Before each test, a load cell was connected to a multimeter and used to check the exact lever arm ratio for calibration of the stress. A linear variable differential transformer (LVDT) was used to measure the displacement during the creep test, which was also calibrated before each test.

The test cylinder, the SiC blocks, and all surfaces of the creep fixtures inside the furnace were coated with boron-nitride (BN) spray, a hightemperature lubricant. The cylinder was placed between the SiC blocks and centered inside the compression fixtures. A small preload (<1 MPa) was placed on the weight pan to ensure the specimen would remain in place for the remainder of the set-up. The furnace was closed around the frame, and extra insulation was used to fill any gaps in the furnace to keep the temperature stable during the test. A ramp rate of 5 $^{\circ}$ C/min was used to heat the specimens to the testing temperature. At least 1 h was held before beginning the test to ensure the stabilization of the temperature. To begin the test, the weight was loaded to the first desired stress and the data collection was started. As the creep specimen strained during the test, a proximity sensor on the lever arm tripped, and the lower crosshead moved down to always keep the lever arm level. The data was monitored and examined periodically during the test. When the strain vs. time plot showed a clear linear slope, the stress was increased by approximately 1-5 MPa depending on the temperature. Each time more weight was added to the weight pan, the date and time were recorded. The creep tests were stopped when a total of up to 8–10% strain was achieved in the specimen. The test was repeated for

temperatures at 275, 300, 325, 350, 375, and 400 °C. It is noted that the compressive loading direction is perpendicular to the build direction of the LPBF samples, as shown in Fig. 1(b).

2.3. Microstructural characterization

Microstructural characterization was performed on as-built and all crept Al-10Ce specimens. These specimens were sectioned using a lowspeed diamond saw along the XZ plane of the cylinder, as shown in Fig. 1 (b). The specimens were mounted in epoxy resin, and their crosssections were ground until plane using SiC sandpapers up to 1200 grit. They were then polished first by using $1 \mu m$ diamond pastes followed by the 0.05 µm colloidal silica suspensions until no scratches remained on the surface. Immediately after polishing, the specimens were etched using Keller's reagent. A scanning electron microscope (JEOL JSM 6510LV) operating at 20 kV was used to observe the microstructure. All specimens were also tested for hardness using a Buehler Micromet 5101 Micro Hardness Tester. The test force used was 2.942 N, and the hardness was calculated by taking an average across five measurements for each specimen. Electron backscatter diffraction (EBSD) was performed on the as-built specimen and specimens crept at 325 °C and 400 °C to determine the grain size and crystallographic orientation. The FEI Scios SEM equipped with the EDAX Hickory EBSD system and version 8 of the TSL-OIM software was used for the EBSD analysis. The surface of all specimens was repolished using 0.05 µm colloidal silica suspensions before EBSD measurement. The Al-rich FCC matrix was used to index the EBSD pattern and the grain size was calculated considering the average circular equivalent diameter.

3. Results and analysis

3.1. As-built microstructure

Fig. 2 presents the etched optical and backscatter electron (BSE) micrographs of the as-built alloy along its XZ cross-section. The typical "fish-scale" type of melt pools due to laser-material interaction are observed. The low magnification BSE micrograph in Fig. 2(b) showed melt pool boundary and faint signs of grain boundary. The high magnification BSE micrograph in Fig. 2(c) showed very fine scale of eutectic Al + Al₁₁Ce₃ microstructure, albeit it is slightly coarser along the melt pool boundary than inside the melt pool. Some directional growth of the eutectic microstructure perpendicular to the melt pool boundary was also observed because of thermal gradient during solidification. The eutectic feature is consistent with the previous transmission electron microscopic observation, which showed that the asbuilt alloy exhibits a eutectic Al + Al $_{11}$ Ce $_{3}$ network structure at the nanometer scale, i.e., the thickness of Al₁₁Ce₃ ribbons is less than 50 nm [19]. Overall, the bar specimen for subsequent creep testing shows little porosity and fine microstructure, which is consistent with the results from a small cubic sample manufactured using the same processing parameters [19].

3.2. Creep property

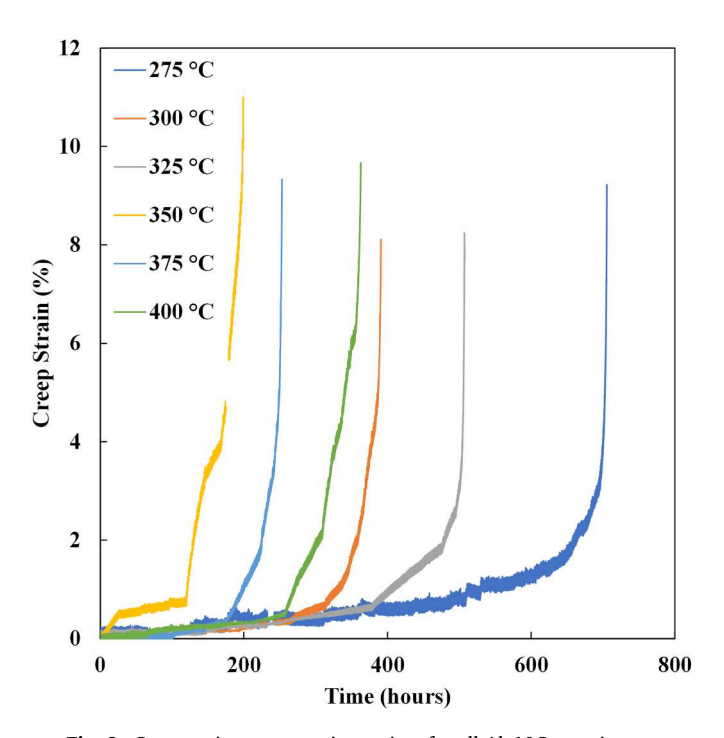
Fig. 3 shows the strain (ε) vs time (t) curve for all compressive creep tests from the cylindrical Al–10Ce specimens. Due to the nature of stress incremental creep test, the strain increases at an incremental rate during the test duration. This is reflected in the stepwise curves in Fig. 3, with a much larger apparent slope near the end of each test due to higher applied load. Various testing time is needed before an accumulation of near 10% strain is approached. Table 1 shows the different testing duration for each testing temperature. For the specimen tested at the lowest temperature of 275 °C, the testing time is about 705 h, indicating an isothermal heat treatment under various stresses for nearly a month.

For each linear segment, the minimum creep strain rate $(\dot{\epsilon})$ was determined from the calculated slope. Fig. 4 presents the strain rate vs stress (σ) in a log-log plot for each compressive creep test. For example, the dark blue dots in Fig. 4 indicate that the minimum strain rate ranges approximately from 2.3×10^{-10} to 1.2×10^{-5} s⁻¹ as the stress increased from 20 to 110 MPa at 275 °C.

The steady state creep strain rate can be described by the phenomenological power-law relationship, expressed as:

$$\dot{\varepsilon} = A\sigma^n \exp\left(\frac{-Q}{RT}\right) \tag{1}$$

where A is a material constant, n is the creep stress exponent, and Q is the creep activation energy, σ is the creep stress, R is the gas constant



 $\textbf{Fig. 3.} \ \ \text{Compressive creep strain vs. time for all Al-10Ce specimens.}$

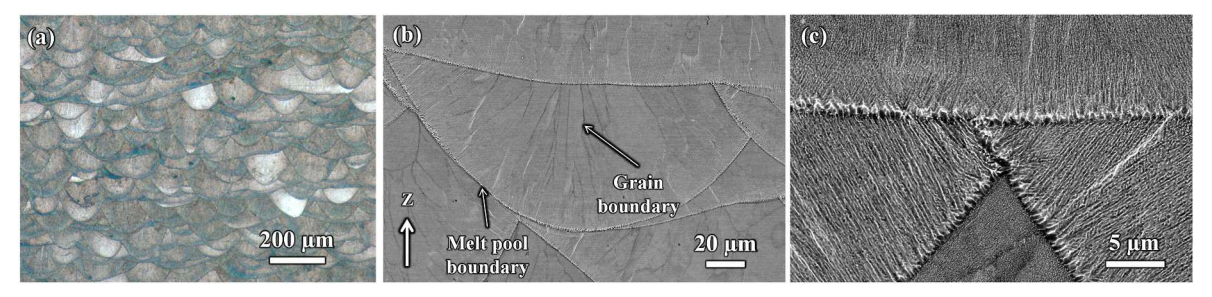


Fig. 2. (a) Optical micrograph, (b) low magnification and (c) high magnification backscatter electron micrograph of the as-built Al-10Ce alloy.

Table 1
Compressive creep testing conditions including temperature, stress range, and time and measured Vickers hardness for each specimen after test.

Specimen ID	As-built	1	2	3	4	5	6
Temperature (°C)	N/A	275	300	325	350	375	400
Stress (MPa)	N/A	20-110	10-75	10-70	15-45	2.5-35	4.5-17.5
Time (hours)	N/A	705	390	508	200	253	363
Vickers Hardness (HV)	97.2 ± 3.2	71.6 ± 2.1	66.4 ± 2.3	60.6 ± 2.2	58.2 ± 3.3	59.3 ± 3.7	58.9 ± 0.9

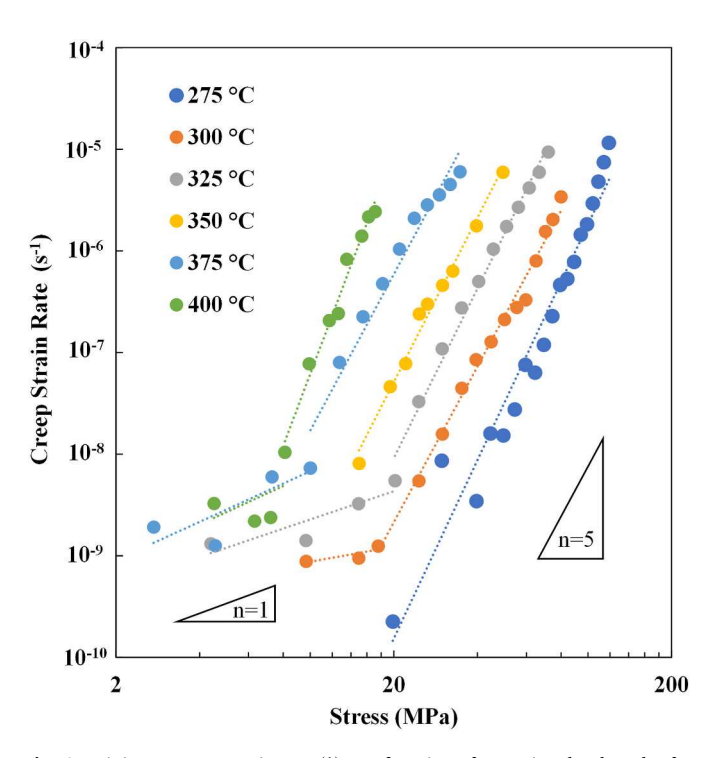


Fig. 4. Minimum creep strain rate $(\dot{\varepsilon})$ as a function of stress in a log-log plot for all Al–10Ce specimens.

and T is the temperature. In a $log \dot{e} - log \sigma$ curve, Eq.~(1) is represented by a linear line with the slope equal to n. This can be calculated from the fitted curves for various temperatures following expression:

$$n = \frac{d \log \dot{\varepsilon}}{d \log \sigma} \tag{2}$$

Several curves in Fig. 4 show two distinct linear segments, and therefore two different n values were calculated and reported as $n_{diffusion}$ for lower stresses and $n_{dislocation}$ for higher stresses, as listed in Table 2. The $n_{diffusion}$ values at lower stresses are approximately equal to 1, which indicate that the diffusion creep is the dominate deformation mechanism. The $n_{dislocation}$ values at higher stresses range between 5 and 7.5, which indicate dislocation creep as the main deformation mechanism. The $n_{disfusion}$ was not reported for specimens tested at 275 and 350 °C, probably because they were not tested at stresses low enough to result in clear diffusion creep.

For high purity Al, the stress exponent is measured to be n = 4.4 and the creep activation energy is approximately $Q_{Al} = 142$ kJ/mol over the

Table 2Creep stress exponents and threshold stress at various temperatures.

Temperature (°C)	$n_{diffusion}$	$n_{dislocation}$	Threshold Stress (MPa)
275	N/A	5.8	51.2
300	1.1	5.1	23.3
325	0.9	5.4	17.8
350	N/A	5.5	11.8
375	0.9	5.2	7.3
400	1.3	7.4	6.3

temperature ranging from 260 to 590 °C [28]. The higher stress exponent $n_{dislocation}$ in the Al–10Ce alloy than that of the pure aluminum for dislocation creep indicates the presence of some threshold stress. To account for the threshold stress (σ_{th}), Eq.~(1) can be rewritten as:

$$\dot{\varepsilon} = A'(\sigma - \sigma_{th})^n \exp\left(\frac{-Q}{RT}\right)$$
(3)

The threshold stress for each temperature is determined by fitting the curve of $\dot{\varepsilon}^{\frac{1}{44}}$ vs stress for each temperature using a least squares linear regression. The threshold stress is obtained by extrapolating the fitted lines to $\dot{\varepsilon}=0$, as listed in Table 2. The threshold stress represents the inability of dislocations to climb over the precipitates at low stresses. Since n=4.4 represents the dislocation creep in pure Al, normalizing the curve using this value for the stress exponent isolated the effect of the fine eutectic $Al_{11}Ce_3$ in inhibiting the dislocation movement during creep deformation.

At a given stress, the creep activation energy can be determined from *Eq.* (1) as:

$$Q = -R \left(\frac{dln\dot{\varepsilon}}{d\left(\frac{1}{T}\right)} \right) \tag{4}$$

Fig. 5 presents the strain rate vs. temperature curve using the $ln\dot{e}-1/T$ at several compressive stresses. The activation energy was calculated to be 244.3, 218.2 and 223.2 kJ/mol·K for stress of 24.5, 29 and 50 MPa, respectively. Therefore, the average activation energy was found to be approximately 228.6 kJ/mol·K for dislocation creep in the temperature range from 275 to 375 °C.

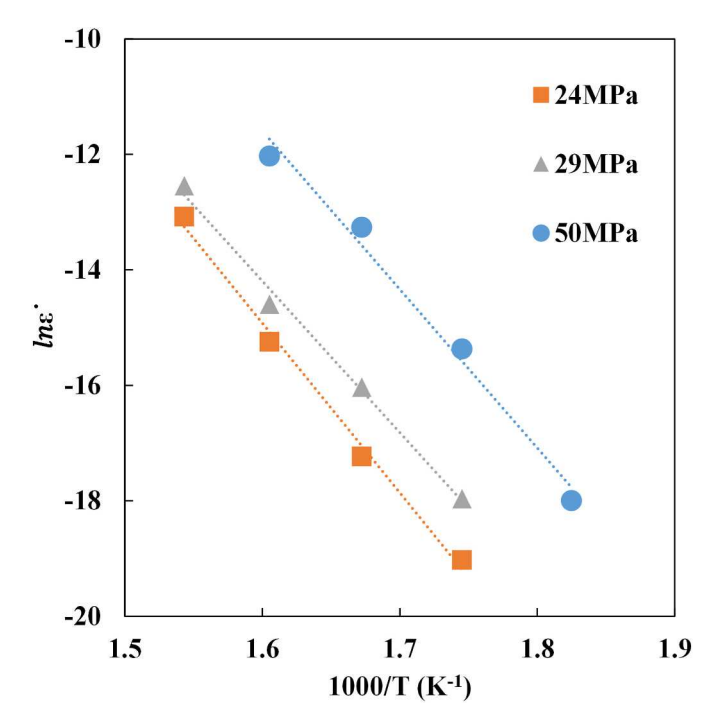


Fig. 5. Estimation of creep activation energy at three different creep stresses.

3.3. Microstructural evolution

Figs. 6 and 7 show the BSE micrographs for the evolution of the microstructure after the compressive creep tests. It is noted from Fig. 1 that the XZ cross-section parallel to the build direction is characterized. Compared to the as-built specimen, all crept specimens showed spheroidization and coarsening of the intermetallic Al₁₁Ce₃ phases to different levels. A direct comparison across specimens crept at different temperatures is difficult due to the different amount of testing time. Generally, as temperature increased, the melt pool boundaries faded, while the grain boundaries became more pronounced. At lower temperatures such as 275 °C, the Al₁₁Ce₃ intermetallics agglomerated and coarsened slightly and they were still distributed throughout the matrix. The high magnification BSE micrographs in Fig. 7(a) indicated that spheroidization of some Al₁₁Ce₃ intermetallics occurred within the melt pool, yet the size of them remained in the nanometer range. The coarsening of the $Al_{11}Ce_3$ intermetallics due to Ostwald ripening was more pronounced along the grain boundaries as the temperature increased. The high magnification BSE micrograph in Fig. 7(f) of crept specimen at 400 °C showed that some of the larger intermetallics grew to approximately 2-3 µm in diameter, particularly along the grain boundary. The rapid grain boundary diffusion contributes to the faster coarsening rate of the intermetallics along the grain boundary than within the grains.

In all crept specimens, the region along grain boundaries appeared darker than the grain interior compared to the as-built state as shown in Fig. 7. EDS was performed within the grains, at the Al₁₁Ce₃ intermetallic and at the dark spot along the grain boundary. The EDS results indicated that there was a deficit of Ce in the darker area near the grain boundary region, so that the region along the grain boundaries is nearly pure Al decorated by coarsened Al₁₁Ce₃ intermetallics after creep deformation. Some of these Ce-depleted region are nearly $4-5 \mu m$ in width across the grain boundary, as shown in Fig. 7. It is also noticed that these regions align preferentially along the vertical grain boundaries, which formed nearly parallel to the build direction. Since the compressive stress was applied out of plane in Fig. 7, the Ce-depleted region is perpendicular to the compressive stress and thus their thickening corresponds to the lateral expansion direction of the crept specimen. This indicates that there is migration of Al atoms toward the vertical grain boundaries. The microstructure is similar to denuded zone that was observed in other materials, such as Mg-rare earth alloys [29,30] and superalloys [31,32], that undergo creep deformation. The exact formation mechanism of denuded zones remains debatable [33], but is believed to be induced by

directional diffusion flow [34] or grain boundary sliding/migration during the creep deformation [34]. In the present crept specimens that underwent incremental levels of stress and thus different deformation mechanisms, it is difficult to clarify the mechanisms until further dedicated experiments are performed.

Fig. 8 present the EBSD inverse pole figure maps (IPF-Z) of the asbuilt specimen and specimens tested at 325 and 400 °C. Similar to many other LPBF Al alloys, Al–10Ce alloy developed a microstructural and crystallographic texture. In the as-built specimen, microstructural texture can be observed by the general columnar grain morphology, which formed a fan-like structure within the melt pool and mainly aligned with the build direction. The corresponding pole figures indicate a weak cube texture as manifested by the concentrated contours near the north and south poles in the (001) pole figure. Similar information can be seen from the inverse pole figures with respect to the specimen directions. This indicates that some of the crystallographic <001> orientations of the as-built Al–10Ce alloy preferentially grow toward the build direction because of the strong thermal gradient along the build direction during the cooling process.

Compared to the as-built specimen, the grains in the crept specimens are still primarily columnar in shape with their long edges aligned closely to the build direction. Fig. 9 shows the grain size distribution of the three specimens, which indicates little difference between the three specimens. The average grain diameters in terms of equivalent area are 23.4, 24.9 and 24.6 μm for the as-built specimen, specimen tested at 325 °C for 508 h, specimen tested at 400 °C for 363 h, respectively. The average aspect ratio of the grain is 0.42, 0.45 and 0.48, respectively. Both the average grain size and aspect ratio only increased slightly after prolonged creep test, indicating that grain growth or dynamic recrystallization was negligible in the Al–10Ce alloy.

After creep deformation, the pole figures and inverse pole figures remain nearly the same with little changes in the density distribution. This indicates that no major changes in grain orientation distribution occurred during creep deformation, which is consistent with the observation that grain size and shapes also remained stable.

The Vickers hardness of all specimens is listed in Table 1. All crept specimens showed a reduction in hardness value compared to the asbuilt specimen, for example, the hardness decreased by 40% after creep deformation at 400 $^{\circ}$ C for 363 h. This can be attributed to loss of fine eutectic structure due to coarsening. As a comparison, the hardness of 58.9 for the specimen crept after 363 h of 400 $^{\circ}$ C was still more than 50% higher than the hardness of the as-cast Al-12.5Ce alloy [23].

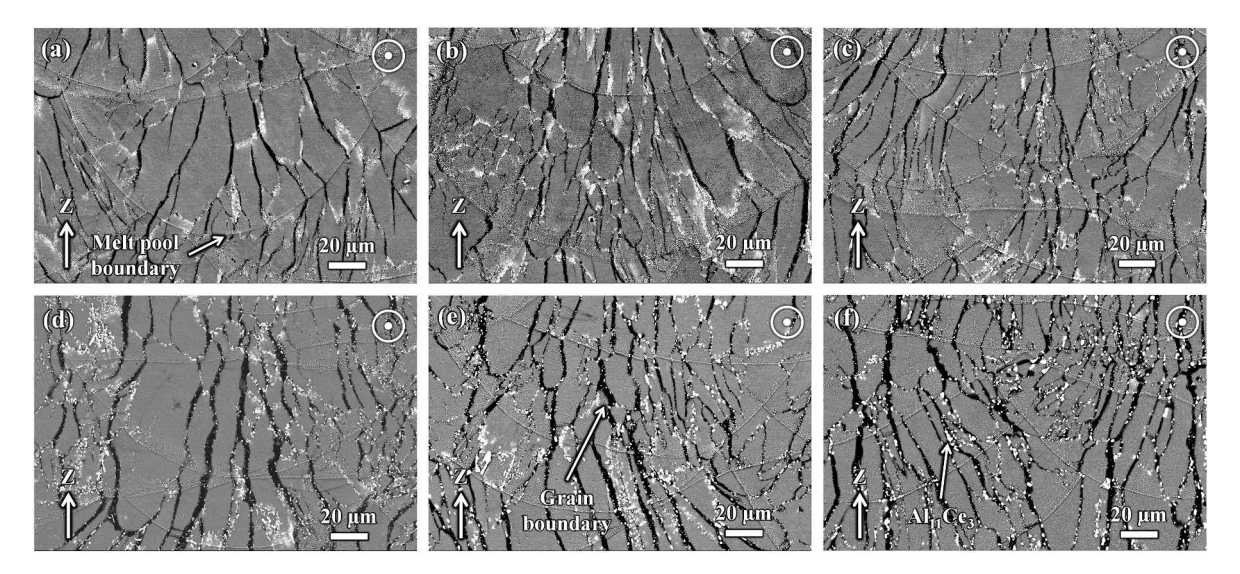


Fig. 6. Backscatter electron micrographs of the crept specimens: (a) 275 °C and 705 h, (b) 300 °C and 390 h, (c) 325 °C and 508 h, (d) 350 °C and 200 h, (e) 375 °C and 253 h, (f) 400 °C and 363 h. The compressive loading direction is out of plane as indicated in the upper right corner.

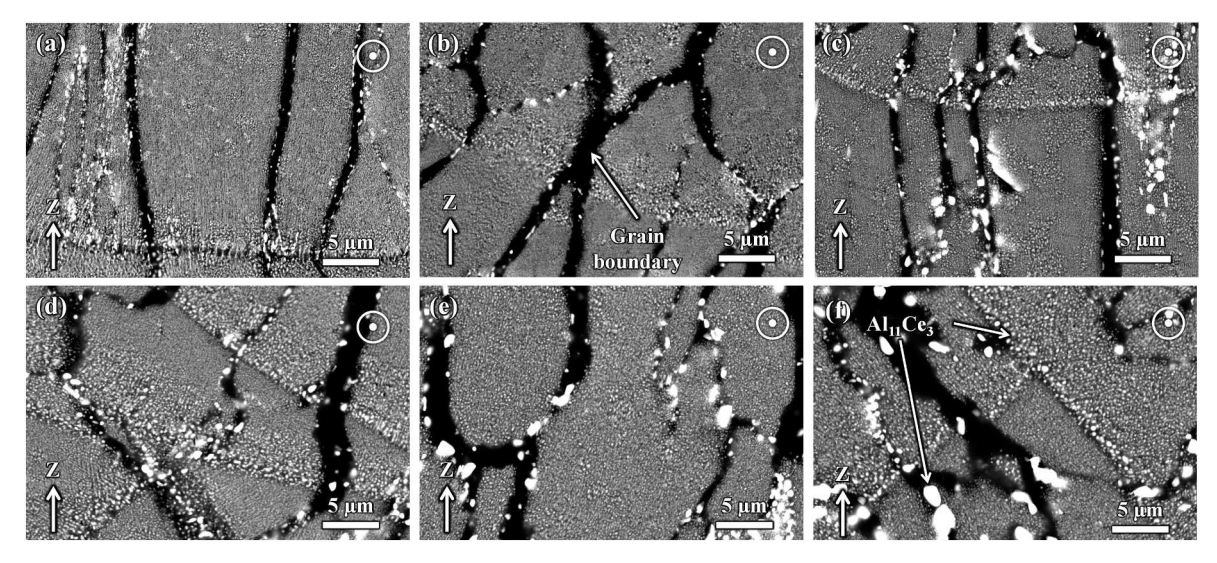


Fig. 7. High magnification backscatter electron micrographs of the crept specimens: (a) 275 °C and 705 h, (b) 300 °C and 390 h, (c) 325 °C and 508 h, (d) 350 °C and 200 h, (e) 375 °C and 253 h, (f) 400 °C and 363 h. The compressive loading direction is out of plane as indicated in the upper right corner.

4. Discussions

For the first time, this study measured the minimum creep strain rate and investigated the microstructural evolution during creep for the LPBF binary near-eutectic Al–10Ce alloy, which provides a benchmark creep property for Al–Ce based alloys manufactured by LPBF. Comparisons to the creep property of other cast or LPBF Al alloys will be discussed and development of creep resistant Al–Ce alloys will be suggested.

4.1. Compared to cast Al-Ce alloys

Cast Al-Ce based alloys showed excellent castability and decent strength, and could potentially be a substitute for Al-Si based alloys for automotive applications. Several recent studies have reported their creep properties and selected results are summarized in Table 3. Fig. 10 (a) presents the creep strain rate measured at 300 °C superimposed with that of the LPBF Al-10Ce at same temperature from this study. Liu. et.al. [23] studied the cast Al-12.5Ce, which is near-eutectic but has a slightly higher Ce content than this study. At relatively low stresses, the difference of the strain rates between the LPBF and cast alloys is small, indicating that the diffusional creep deformation due to vacancy or atomic diffusion occurs at a similar rate through the lattice or the grain boundary. However, it is observed that the LPBF alloy is more creep resistant than the cast alloy as the stress magnitude increases. At stress of about 55 MPa, the strain rate is almost two orders of magnitude lower in the LPBF alloy. This indicates that the fine and uniformly distributed Al₁₁Ce₃ intermetallics in LPBF alloys are more effective than the blocky Al₁₁Ce₃ intermetallics in cast alloys in inhibiting the dislocation movement when the dislocation creep dominates.

With additional alloying elements, some higher-order cast Al–Ce alloys show improved creep resistance. With addition of 5 wt% Ni, Wu et al. showed that the improved creep resistant in cast near-eutectic Al–10Ce–5Ni alloy can be attributed to the enhanced load transfer from increased volume fraction of intermetallics [11]. Cast Al–12Ce-0.4Sc alloy showed lower creep strain rate than the LPBF Al–10Ce alloy. Yi et al. showed that the addition of Sc results in uniform distribution of Al₃Sc precipitates and introduces additional lattice misfit strain that inhibits the dislocations to climb [35]. Compared to the Al-7.3Ce-0.22Sc-0.09Zr alloy [36], both alloys showed similar diffusion creep strain rates at low stresses, while their strain rate curves crossed over due to the higher stress exponent in the cast Al-7.3Ce-0.22Sc-0.09Zr alloy. However, the LPBF alloy outperforms the cast hypoeutectic Al-6.9Ce-9.3 Mg [24] despite its strong solid solution

strengthening from Mg. It was observed that the hypoeutectic composition consists of large areas with fast creeping Al–Mg solid solution matrix, which contributes to the inferior creep property. In contrast, the LPBF Al–10Ce consists of a uniform eutectic microstructure throughout the matrix without any weak regions. Similarly, the LPBF also is more creep resistant than the hypoeutectic Al–6Ce–3Ni-0.7Fe alloy [37]. Despite its overall higher volume fraction of intermetallics, the alloy has weaker Al dendrites and coarser intermetallics than the LPBF binary alloy. Overall, it seems that more volume fraction of intermetallics and formation of precipitates increase the stress exponent.

4.2. Compared to LPBF Al-Ce alloys

The creep study on Al–Ce based alloys manufactured by LPBF has been limited up to date, and the minimum strain rate of them is presented in Fig. 10(b). Rakhmonov et al. [25] reported the creep behavior of LPBF Al–7Ce–8Mg alloy, which is inferior to LPBF Al–10Ce alloy especially as the stress magnitude increases. Although room temperature strength of LPBF ternary Al–Ce–Mg is higher than binary Al–Ce alloy [21,22,25,42], the rapid diffusing Al–Mg solid solution may facilitate the dislocation climb over the fine precipitates at high temperature, and thus lowers the creep resistance. Michi et al. reported the creep property of LPBF quaternary Al-10.5Ce-3.1Ni-1.2Mn [26]. With the addition of Ni and Mn, the quaternary alloy outperforms the binary composition with a much lower strain rate at higher stresses. The much higher volume fraction of submicron intermetallics in the quaternary alloy compared to the binary alloy (~35% [26] vs. ~11.8% [19]) accounts for its high strength and creep resistance.

4.3. Compared to LPBF AlSi10Mg alloys

AlSi10Mg alloy is currently the benchmark Al alloy extensively used in LPBF. This alloy also has a near-eutectic composition and generally forms a fine cellular microstructure in the as-built state. The small amount of Mg (<0.5 wt%) will contribute to the strength through precipitation hardening after T6 heat treatment [43,44], which leads to a higher room temperature tensile strength than LPBF Al–10Ce alloy. However, the rapid diffusion of Si and Mg in Al matrix results in rapid coarsening of the microstructure and precipitates, which deteriorates the high temperature property of AlSi10Mg alloy [45]. Several studies reported the creep property of LPBF AlSi10Mg alloys recently. Fig. 10(c) summarizes the minimum strain rate vs. stress for LPBF AlSi10Mg alloys found in literature, where the testing conditions expand over a wide

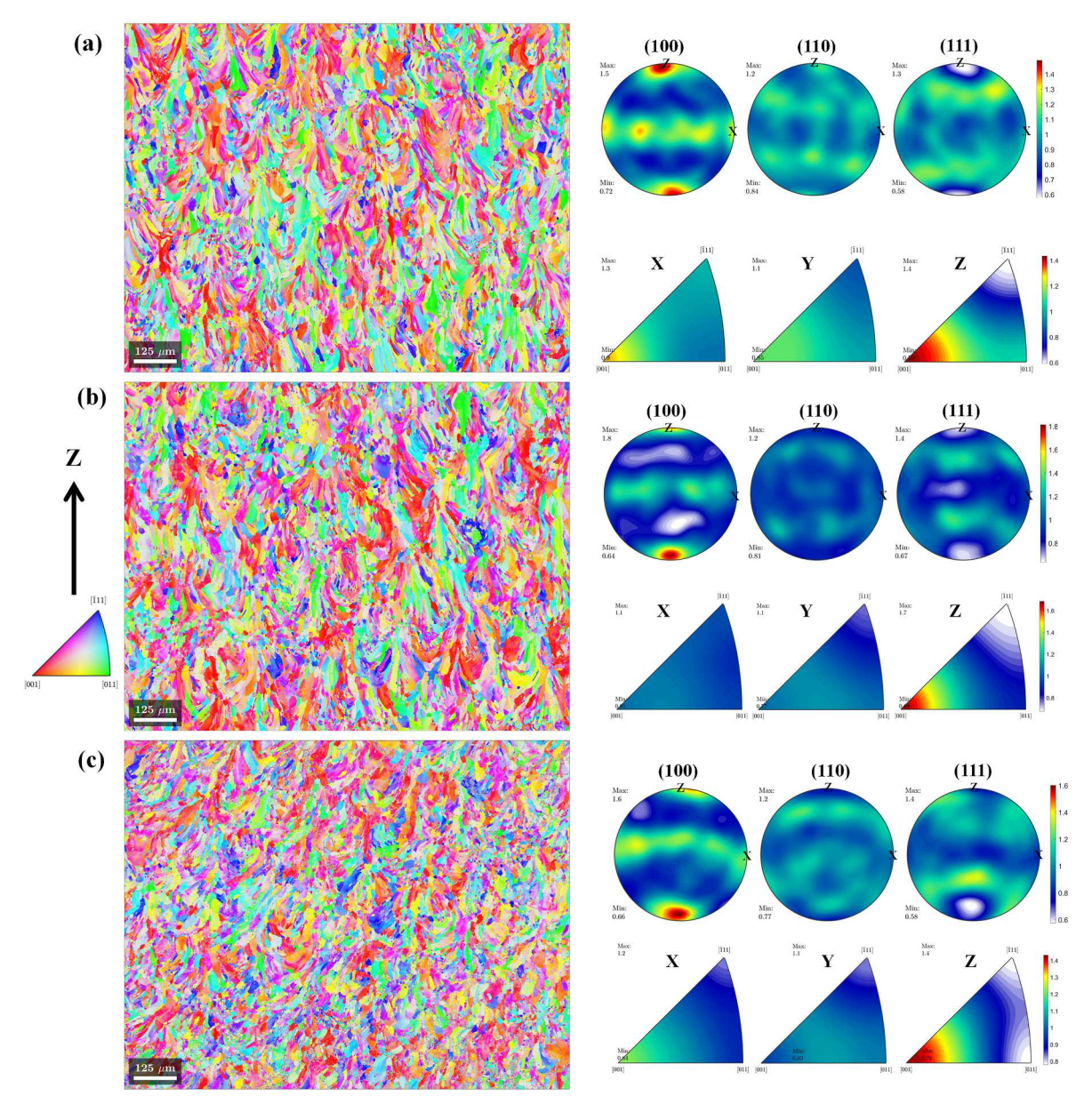


Fig. 8. Inverse pole figure maps with respect to the Z direction (IPF-Z) for (a) as-built specimen and crept specimens tested at (b) 325 °C for 508 h and (c) 400 °C for 363 h. The corresponding (100) (110) and (111) pole figures are shown below the IPF-Z maps.

range of temperatures and stresses. The minimum strain rate for the LPBF Al-10Ce measured from this study at 300 °C is superimposed for comparison. At 300 °C, the minimum strain rate of LPBF Al-10Ce is one to two orders of magnitude lower than that of the LPBF AlSi10Mg measured by Glerum et al. [38] and Fiedler et al. [41]. It is noted that the creep test from Glerum et al. [38] is highly comparable to this study: both studies measured the compressive minimum strain rates perpendicular to the LPBF build direction. The stress exponent n is generally higher in LPBF AlSi10Mg alloy, regardless of the measuring range. Glerum et al. [38] and Fiedler et al. [41] reported a stress exponent of approximately n = 10-13 and n = 7-8, respectively, which is slightly higher than that of Al-10Ce within similar stress range. Paoletti et al. [39] and Uzan et al. [40] reported $n = 18 \sim 25$ for AlSi10Mg alloy, which is measured at a much lower temperature and very high stress range. Furthermore, breakdown of the Si cellular network [38-40] was observed even after crept at lower temperature and shorter duration compared to the current study. The Si coarsens into blocky particles with $2-3 \mu m$ in size after 1 month of exposure to 260 °C [38], yet Fig. 7 shows that $Al_{11}Ce_3$ remains submicron in size after 1 month of exposure to 275 °C. Both the low solubility and slow diffusivity of Ce in Al contribute to the slow coarsening rate in Al–10Ce alloy. Overall, binary LPBF Al–10Ce alloy, despite lacking strengthening precipitates compared to LPBF AlSi10Mg, still exhibits superior creep deformation resistance and microstructural stability at high temperatures.

4.4. Alloy development

Based on the results of this study and comparisons with recent literature, several general implications can be deduced for developing and manufacturing creep-resistant Al–Ce based alloys. First of all, refining the intemeratllics can improve the creep resistance. The LPBF with significantly faster cooling rate promotes the refinement of Al–Ce based intemetallics compared to the cast alloys [19,21,22,37,46], and thus improve the creep resistance by impeding the dislocation movement. Fortunately, of all the Al–Ce-based alloy investigated by LPBF up to date, all of them exhibit an outstanding printability without any

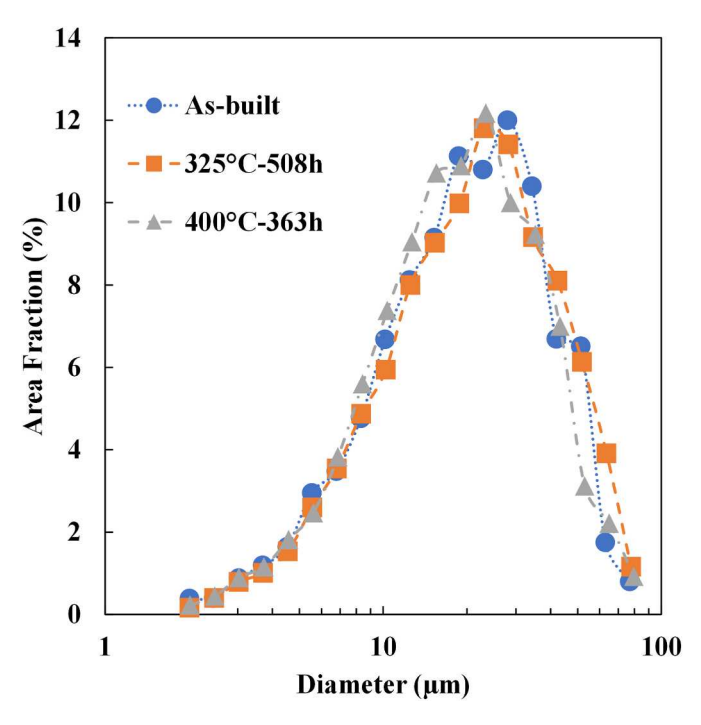


Fig. 9. Grain size distribution for as-built specimen and crept specimens tested at 325 $^{\circ}\text{C}$ for 508 h and 400 $^{\circ}\text{C}$ for 363 h.

evidence of solidification cacking [12,19-22,25,26,42,46-48]. It is noted that most of them are based on either binary or ternary eutectic or hypoeutectic compositions that inherently have low cracking tendency [18]. Second, increasing the volume fractions of the intermetallics can further improve the creep resistance by slowing down dislocation creep and providing load transfer. Some transition alloying elements such as Ni, Mn and Fe have been shown to increase the volume fraction of intermetallics in Al-Ce alloys [20,26,37]. They either form higher order intermetallics together with Ce or simply form other intermetallics without Ce. These complicated intermetellics are a result of various solidification reactions during the solidification process, and more thermodynamic modeling and precipitates characterizations are still needed to understand them. Another approach to increase the volume fraction of intermetallics is to increase the Ce concentration to possibly the hypereutectic range, which has not been explored up to date. Yet, the effect of the increased volume fraction of intermetallics on the creep

ductility remains to be evaluated. Thirdly, elements including Sc and Zr among others that form Al₃X type of precipitates with L1₂ crystal structure can also be beneficial to creep property of Al-Ce alloy through Orowan strengthening [36]. Currently no ternary Al-Ce-Sc or Al-Ce-Zr intermetallics have been reported, therefore it is expected that alloying of Sc or Zr either goes into solid solution or forms Al₃X precipitates [49, 50]. On the other hand, LPBF Al alloys with Sc and Zr have shown significantly refined grains [16,51,52], which may negatively impact the creep property as the grain boundary area increases. Further research is still needed to understand the extent of potential grain refinement in Al-Ce alloy by Sc and Zr addition and its effect on creep property. Last but not least, certain alloying elements such as Mg may need to be restricted in creep-resistant Al-Ce alloys. Research has shown that Mg increases the room temperature strength at the sacrifice of ductility [10,22]. However, at high temperature, the rapid diffusivity of Mg in Al accelerates the creep rate by promoting the diffusion creep and dislocation climb creep [24]. The primary Al-Mg solid solution phase particularly in hypoeutectic Al-Ce-Mg alloy is the creep-weak region that lowers the overall creep-resistance [24]. Additionally, high concentration of Mg has been observed to degrade the printability of Al-Ce alloy due to excessive vaporization and slag generation associated with its high vapor pressure [21,22].

5. Summary

The study investigated the microstructural evolution and creep property of a near eutectic binary Al–10Ce alloy manufactured by LPBF for the first time, which serves as a benchmark alloy for future development of creep-resistant alloy based on Al–Ce compositions. The main findings are summarized below.

- As-built Al–10Ce alloy exhibited columnar grains having an average equivalent diameter of approximately 23 μm . The long axis of the grains aligned closely to the build direction and showed a weak cube texture. The microstructure consisted of eutectic Al + Al $_{11}$ Ce $_{3}$ with fine Al $_{11}$ Ce $_{3}$ intermetallics in the nanometer size range. The microstructure along the melt pool boundary is slightly coarser than that within the melt pool.
- Compressive creep tests with incremental stresses were performed on LPBF Al–10Ce alloy between 275 and 400 °C. The stress exponent was n=1 at low stress regime indicating diffusion creep, and n=5–7 at high stress regime indicating dislocation creep. The average activation energy was approximately 229 kJ/mol·K in the temperature between 275 and 375 °C. Compared to the cast Al–Ce alloy with

Table 3
Creep stress exponent and activation energy for various cast and LPBF Al–Ce based alloys and LPBF AlSi10Mg alloy from literature.

Alloy	Temperature (°C)	Stress (MPa)	Stress exponent, n	Activation energy (kJ/mol·K)	Approximate stress resulting in a 10^{-7} s $^{-1}$ strain rate at 300 $^{\circ}$ C	Reference
Al-10Ce	275-400	3–110	5–7.5	231	41	LPBF, this study
Cast Al-12.5Ce	260-350	12-70	9–11	215	31	Liu, as-cast, compressive [23]
Al-10Ce-5Ni	300	20-70	12	N/A	45	Wu, as-cast, compressive [11]
Al-12Ce-0.4Sc	300	55-80	23-32	N/A	66	Yi, cast and aged, tensile [35]
Al-6.9Ce-9.3 Mg	300-400	5-66	4–5	246	16	Ng, compressive [24]
Al-6Ce-3Ni-0.7Fe	300	20-58	12	N/A	31	Wu, as-cast, compressive [37]
Al-7.3Ce-0.22Sc-0.09Zr	300	20-65	16-18	N/A	46	Ekaputra, as-cast, compressive
						[36]
Al-6.9Ce- 0.027Sc-	300	20-48	11-13	N/A	31	Ekaputra, as-cast, compressive
0.20Zr-0.017Er						[36]
Al-7.3Ce-7.7 Mg	300	10-50	8.5	N/A	32	Rakhmonov, LPBF and aged,
						compressive [25]
Al-10.5Ce-3.1Ni-1.2Mn	300-400	10-80	6-12	189-264	N/A (>80)	Michi, LPBF, tensile [26]
AlSi10Mg	260-300	10-70	6-13	256	19	Glerum, LPBF, compressive
						[38]
AlSi10Mg	150-205	125-300	18-24	200	N/A	Paoletti, LPBF, tensile [39]
AlSi10Mg	225-300	117-147	25	146	N/A	Uzan, LPBF, tensile [40]
AlSi10Mg	300	18-53	7–8	N/A	18	Fiedler, LPBF, compressive
						[41]

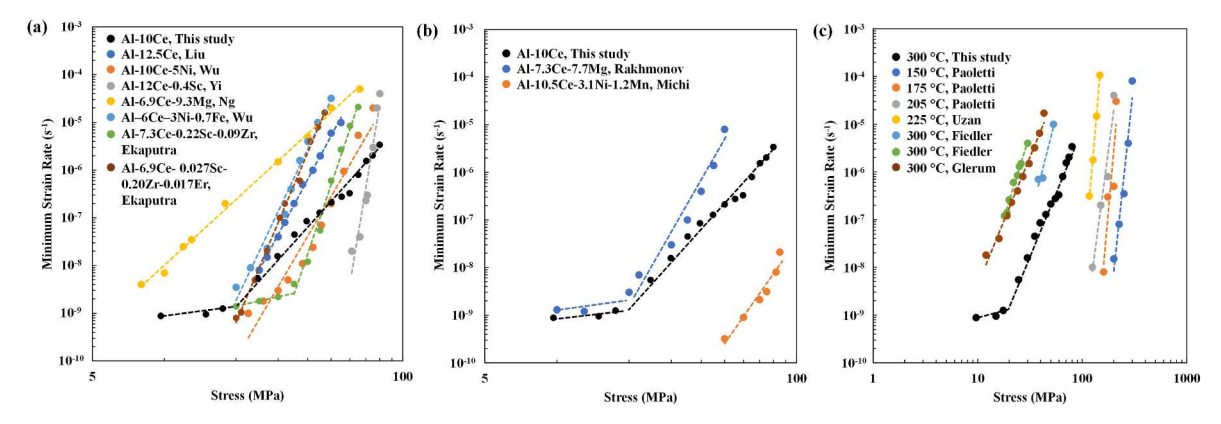


Fig. 10. Minimum creep strain rate $(\dot{\epsilon})$ as a function of stress in a log-log plot for (a) various cast Al–Ce-based alloys tested at 300 °C [11,23,24,35–37], (b) various LPBF Al–Ce-based alloys tested at 300 °C [25,26], (c) LPBF AlSi10Mg alloys tested at various temperatures [38–41].

similar composition, LPBF Al–10Ce has much lower minimum creep strain rates especially as the stress increases. Compared to the LPBF AlSi10Mg alloy, the minimum creep strain rate is nearly two orders of magnitude lower in LPBF Al–10Ce alloy. LPBF Al–10Ce alloy is also more creep resistant than cast and LPBF ternary Al–Ce–Mg alloys, suggesting Mg may be detrimental to creep resistance in Al–Ce alloy. The quaternary LPBF Al-10.5Ce-3.1Ni-1.2Mn alloy is more creep resistant than the LPBF Al–10Ce alloy, suggesting higher volume fraction of intermetallics due to alloying of Ni and Mn is beneficial to creep resistance.

 \bullet The LPBF Al–10Ce alloy is thermally stable after long time creep testing. The melt pool boundary faded while the grain boundaries were more pronounced as creep temperature increased. The grain size, distribution and crystallographic texture remained relatively unchanged, indicating little dynamic recrystallization at temperatures up to 400 $^{\circ}$ C. The Al $_{11}$ Ce $_{3}$ intermetallics slightly coarsened to different levels depending on the temperature, both within the grains and along the grain boundary.

Author statement

Jillian Stinehart: Conceptualization, Methodology, Investigation, Formal analysis, Writing- Original draft preparation. Luis Fernando Ladinos Pizano: Investigation, Formal analysis. Wei Xiong: Writing-Reviewing and Editing. Le Zhou: Conceptualization, Supervision, Writing- Original draft preparation, Writing- Reviewing and Editing, Funding acquisition.

Declaration of competing interest

The authors declare that they have no known competing financial interests or personal relationships that could have appeared to influence the work reported in this paper.

Data availability

Data will be made available on request.

Acknowledgment

This material is based upon work supported by the National Science Foundation under Grant No. CMMI-2138588. Any opinions, findings, and conclusions or recommendations expressed in this material are those of the authors and do not necessarily reflect the views of the National Science Foundation. The authors would like to thank the Opus college of Engineering at Marquette University for its start-up support. The authors would like to thank Dr. Yongho Sohn from University of Central Florida for providing samples for creep testing and

characterization. The authors would also like to thank Dr. Dinc Erdeniz from University of Cincinnati for helpful discussions on creep testing.

References

- D.N. Seidman, E.A. Marquis, D.C. Dunand, Precipitation strengthening at ambient and elevated temperatures of heat-treatable Al (Sc) alloys, Acta Mater. 50 (2002) 4021–4035.
- [2] K.E. Knipling, D.C. Dunand, D.N. Seidman, Criteria for developing castable, creepresistant aluminum-based alloys–A review, Int. J. Mater. Res. 97 (2022) 246–265.
- [3] D.J. Skinner, R.L. Bye, D. Raybould, A.M. Brown, Dispersion strengthened Al-Fe-V-Si alloys, Scripta Metall. 20 (1986) 867–872.
- [4] Z.C. Sims, O.R. Rios, D. Weiss, P.E. Turchi, A. Perron, J.R. Lee, T.T. Li, J. A. Hammons, M. Bagge-Hansen, T.M. Willey, High performance aluminum–cerium alloys for high-temperature applications, Mater. Horiz. 4 (2017) 1070–1078.
- [5] D. Weiss, Developments in Aluminum-Scandium-Ceramic and Aluminum-Scandium-Cerium Alloys, 2019, pp. 1439–1443.
- [6] F. Czerwinski, Thermal stability of aluminum–cerium binary alloys containing the Al–Al11Ce3 eutectic, Mater. Sci. Eng., A 809 (2021), 140973.
- [7] G. Waterloo, H. Jones, Microstructure and thermal stability of melt-spun Al-Nd and Al-Ce alloy ribbons, J. Mater. Sci. 31 (1996) 2301–2310.
- [8] D. Weiss, Improved high-temperature aluminum alloys containing cerium, J. Mater. Eng. Perform. 28 (2019) 1903–1908.
- [9] R.T. Nguyen, D.D. Imholte, O.R. Rios, D. Weiss, Z. Sims, E. Stromme, S.K. McCall, Anticipating impacts of introducing aluminum-cerium alloys into the United States automotive market, Resour. Conserv. Recycl. 144 (2019) 340–349.
- [10] B. Hu, B. Quan, D. Li, X. Wang, Z. Li, X. Zeng, Solid solution strengthening mechanism in high pressure die casting Al–Ce–Mg alloys, Mater. Sci. Eng. A. 812 (2021), 141109.
- [11] T. Wu, A. Plotkowski, A. Shyam, D.C. Dunand, Microstructure and creep properties of cast near-eutectic Al–Ce–Ni alloys, Mater. Sci. Eng. A. 833 (2022), 142551.
- [12] D.R. Manca, A.Y. Churyumov, A.V. Pozdniakov, A.S. Prosviryakov, D.K. Ryabov, A. Y. Krokhin, V.A. Korolev, D.K. Daubarayte, Microstructure and properties of novel heat resistant Al–Ce–Cu alloy for additive manufacturing, Met. Mater. Int. 25 (2019) 633–640.
- [13] Z.C. Sims, D. Weiss, S.K. McCall, M.A. McGuire, R.T. Ott, T. Geer, O. Rios, P. Turchi, Cerium-based, intermetallic-strengthened aluminum casting alloy: high-volume co-product development, J. Occup. Med. 68 (2016) 1940–1947.
- [14] L. Zhou, H. Pan, H. Hyer, S. Park, Y. Bai, B. McWilliams, K. Cho, Y. Sohn, Microstructure and tensile property of a novel AlZnMgScZr alloy additively manufactured by gas atomization and laser powder bed fusion, Scripta Mater. 158 (2019) 24–28.
- [15] A. Mehta, L. Zhou, T. Huynh, S. Park, H. Hyer, S. Song, Y. Bai, D.D. Imholte, N. E. Woolstenhulme, D.M. Wachs, Additive manufacturing and mechanical properties of the dense and crack free Zr-modified aluminum alloy 6061 fabricated by the laser-powder bed fusion, Addit. Manuf. 41 (2021), 101966.
- [16] L. Zhou, H. Hyer, J. Chang, A. Mehta, T. Huynh, Y. Yang, Y. Sohn, Microstructure, mechanical performance, and corrosion behavior of additively manufactured aluminum alloy 5083 with 0.7 and 1.0 wt% Zr addition, Mater. Sci. Eng. A. 823 (2021), 141679.
- [17] H. Hyer, L. Zhou, A. Mehta, S. Park, T. Huynh, S. Song, Y. Bai, K. Cho, B. McWilliams, Y. Sohn, Composition-dependent solidification cracking of aluminum-silicon alloys during laser powder bed fusion, Acta Mater. 208 (2021), 115(202)
- [18] S. Kou, A criterion for cracking during solidification, Acta Mater. 88 (2015) 366–374.
- [19] L. Zhou, T. Huynh, S. Park, H. Hyer, A. Mehta, S. Song, Y. Bai, B. McWilliams, K. Cho, Y. Sohn, Laser powder bed fusion of Al–10 wt% Ce alloys: microstructure and tensile property, J. Mater. Sci. 55 (2020) 14611–14625.
- [20] A. Plotkowski, K. Sisco, S. Bahl, A. Shyam, Y. Yang, L. Allard, P. Nandwana, A. M. Rossy, R.R. Dehoff, Microstructure and properties of a high temperature

- Al-Ce-Mn alloy produced by additive manufacturing, Acta Mater. 196 (2020)
- [21] K. Sisco, A. Plotkowski, Y. Yang, D. Leonard, B. Stump, P. Nandwana, R.R. Dehoff, S.S. Babu, Microstructure and properties of additively manufactured Al–Ce–Mg alloys, Sci. Rep. 11 (2021) 6953.
- [22] H. Hyer, A. Mehta, K. Graydon, N. Kljestan, M. Knezevic, D. Weiss, B. McWilliams, K. Cho, Y. Sohn, High strength aluminum-cerium alloy processed by laser powder bed fusion, Addit. Manuf. 52 (2022), 102657.
- [23] Y. Liu, R.A. Michi, D.C. Dunand, Cast near-eutectic Al-12.5 wt.% Ce alloy with high coarsening and creep resistance, Mater. Sci. Eng. A. 767 (2019), 138440.
- [24] D.S. Ng, D.C. Dunand, Aging-and creep-resistance of a cast hypoeutectic Al-6.9 Ce-9.3 Mg (wt.%) alloy, Mater. Sci. Eng. A. 786 (2020), 139398.
- [25] J.U. Rakhmonov, D. Weiss, D.C. Dunand, Solidification microstructure, aging evolution and creep resistance of laser powder-bed fused Al-7Ce-8Mg (wt%), Addit. Manuf. 55 (2022), 102862.
- [26] R.A. Michi, K. Sisco, S. Bahl, Y. Yang, J.D. Poplawsky, L.F. Allard, R.R. Dehoff, A. Plotkowski, A. Shyam, A creep-resistant additively manufactured Al-Ce-Ni-Mn alloy, Acta Mater. 227 (2022), 117699.
- [27] L. Zhou, T. Huynh, S. Park, H. Hyer, A. Mehta, S. Song, Y. Bai, B. McWilliams, K. Cho, Y. Sohn, Laser powder bed fusion of Al–10 wt% Ce alloys: microstructure and tensile property, J. Mater. Sci. 55 (2020) 14611–14625.
- [28] O.D. Sherby, P.M. Burke, Mechanical behavior of crystalline solids at elevated temperature, Prog. Mater. Sci. 13 (1968) 323–390.
- [29] W.F. Xu, Y. Zhang, L.M. Peng, W.J. Ding, J.F. Nie, Formation of denuded zones in crept Mg-2.5 Gd-0.1 Zr alloy, Acta Mater. 84 (2015) 317–329.
- [30] X. Dong, L. Feng, S. Wang, G. Ji, A. Addad, H. Yang, E.A. Nyberg, S. Ji, On the exceptional creep resistance in a die-cast Gd-containing Mg alloy with Al addition, Acta Mater. 232 (2022), 117957.
- [31] P.J. Bocchini, C.K. Sudbrack, R.D. Noebe, D.C. Dunand, D.N. Seidman, Microstructural and creep properties of boron-and zirconium-containing cobaltbased superalloys, Mater. Sci. Eng., A 682 (2017) 260–269.
- [32] D.H. Bechetti, J.N. DuPont, J.J. De Barbadillo, B.A. Baker, M. Watanabe, Microstructural evolution of INCONEL® alloy 740H® fusion welds during creep, Metall. Mater. Trans. 46 (2015) 739–755.
- [33] T.G. Langdon, Identifiying creep mechanisms at low stresses, Mater. Sci. Eng., A 283 (2000) 266–273.
- [34] G.W. Greenwood, Denuded zones and diffusional creep, Scripta Metall. Mater. 30 (1994) 1527–1530.
- [35] M. Yi, P. Zhang, C. Yang, P. Cheng, S. Guo, G. Liu, J. Sun, Improving creep resistance of Al-12 wt.% Ce alloy by microalloying with Sc, Scripta Mater. 198 (2021). 113838.
- [36] C.N. Ekaputra, J.U. Rakhmonov, D. Weiss, J. Mogonye, D.C. Dunand, Microstructure and mechanical properties of cast Al-Ce-Sc-Zr-(Er) alloys strengthened by Al11Ce3 micro-platelets and L12 Al3 (Sc, Zr, Er) nanoprecipitates, Acta Mater. 240 (2022), 118354.
- [37] T. Wu, A. Plotkowski, A. Shyam, D.C. Dunand, Microstructure and mechanical properties of hypoeutectic Al-6Ce-3Ni-0.7 Fe (wt.%) alloy, Mater. Sci. Eng., A (2023), 145072.

- [38] J.A. Glerum, J. Mogonye, D.C. Dunand, Creep properties and microstructure evolution at 260–300° C of AlSi10Mg manufactured via laser powder-bed fusion, Mater. Sci. Eng. A. 843 (2022), 143075.
- [39] C. Paoletti, S. Spigarelli, M. Cabibbo, E. Cerri, Creep Behavior of a AlSiMg Alloy Produced by Additive Manufacturing, 2020, pp. 185–193.
- [40] N.E. Uzan, R. Shneck, O. Yeheskel, N. Frage, High-temperature mechanical properties of AlSi10Mg specimens fabricated by additive manufacturing using selective laser melting technologies (AM-SLM), Addit. Manuf. 24 (2018) 257–263.
- [41] T. Fiedler, K. Dörries, J. Rösler, Selective laser melting of Al and AlSi10Mg: parameter study and creep experiments, Progress in Additive Manufact. (2021) 1–10.
- [42] A.A. Martin, J.A. Hammons, H.B. Henderson, N.P. Calta, M.H. Nielsen, C.C. Cook, J. Ye, A.A. Maich, N.E. Teslich, T.T. Li, Enhanced mechanical performance via laser induced nanostructure formation in an additively manufactured lightweight aluminum alloy, Appl. Mater. Today 22 (2021), 100972.
- [43] L. Zhou, A. Mehta, E. Schulz, B. McWilliams, K. Cho, Y. Sohn, Microstructure, precipitates and hardness of selectively laser melted AlSi10Mg alloy before and after heat treatment, Mater. Char. 143 (2018) 5–17.
- [44] J. Fite, S.E. Prameela, J.A. Slotwinski, T.P. Weihs, Evolution of the microstructure and mechanical properties of additively manufactured AlSi10Mg during room temperature holds and low temperature aging, Addit. Manuf. 36 (2020), 101429.
- [45] Y. Cao, X. Lin, Q.Z. Wang, S.Q. Shi, L. Ma, N. Kang, W.D. Huang, Microstructure evolution and mechanical properties at high temperature of selective laser melted AlSi10Mg, J. Mater. Sci. Technol. 62 (2021) 162–172.
- [46] K. Sisco, A. Plotkowski, Y. Yang, D. Leonard, B. Stump, P. Nandwana, R.R. Dehoff, S.S. Babu, Microstructure and properties of additively manufactured Al–Ce–Mg alloys, Sci. Rep. 11 (2021) 6953.
- [47] Z. Yang, C. Chen, D. Li, Y. Wu, Z. Geng, V. Konakov, K. Zhou, An additively manufactured heat-resistant Al-Ce-Sc-Zr alloy: microstructure, mechanical properties and thermal stability, Mater. Sci. Eng. A. 872 (2023), 144965.
- [48] C.N. Ekaputra, D. Weiss, J. Mogonye, D.C. Dunand, Eutectic, precipitationstrengthened alloy via laser fusion of blends of Al-7Ce-10Mg (wt.%), Zr, and Sc powders, Acta Mater. 246 (2023), 118676.
- [49] V. Raghavan, Al-Ce-Zr (Aluminum-Cerium-Zirconium), J. Phase Equilibria Diffus. 31 (2010) 545.
- [50] J.U. Rakhmonov, D. Weiss, D.C. Dunand, Comparing evolution of precipitates and strength upon aging of cast and laser-remelted Al–8Ce-0.2 Sc-0.1 Zr (wt.%), Mater. Sci. Eng. A. 840 (2022), 142990.
- [51] A. Mehta, L. Zhou, T. Huynh, S. Park, H. Hyer, S. Song, Y. Bai, D.D. Imholte, N. E. Woolstenhulme, D.M. Wachs, Additive manufacturing and mechanical properties of the dense and crack free Zr-modified aluminum alloy 6061 fabricated by the laser-powder bed fusion, Addit. Manuf. 41 (2021), 101966.
- [52] L. Zhou, H. Hyer, S. Thapliyal, R.S. Mishra, B. McWilliams, K. Cho, Y. Sohn, Process-dependent composition, microstructure, and printability of Al-Zn-Mg and Al-Zn-Mg-Sc-Zr alloys manufactured by laser powder bed fusion, Metall. Mater. Trans. 51 (2020) 3215–3227.